J. Fluid Mech. (2009), *vol.* 620, *pp.* 31–41. © 2009 Cambridge University Press
doi:10.1017/S0022112008004916 Printed in the United Kingdom

Direct numerical simulations of turbulent flows over superhydrophobic surfaces

MICHAEL B. MARTELL, J. BLAIR PEROT† AND JONATHAN P. ROTHSTEIN

Department of Mechanical and Industrial Engineering, University of Massachusetts,
Amherst, MA 01003, USA

(Received 10 October 2008 and in revised form 6 November 2008)

Direct numerical simulations (DNSs) are used to investigate the drag-reducing performance of superhydrophobic surfaces (SHSs) in turbulent channel flow. SHSs combine surface roughness with hydrophobicity and can, in some cases, support a shear-free air–water interface. Slip velocities, wall shear stresses and Reynolds stresses are considered for a variety of SHS microfeature geometry configurations at a friction Reynolds number of $Re_\tau \approx 180$. For the largest microfeature spacing studied, an average slip velocity over 75 % of the bulk velocity is obtained, and the wall shear stress reduction is found to be nearly 40 %. The simulation results suggest that the mean velocity profile near the superhydrophobic wall continues to scale with the wall shear stress but is offset by a slip velocity that increases with increasing microfeature spacing.

1. Introduction

Significant effort has been placed on the development of surfaces which reduce the amount of drag experienced by a fluid as it passes over the surface. Drag reduction in turbulent flows can be achieved through a number of very different mechanisms including the addition of polymers (Lumley 1969), riblets (Bechert *et al.* 1997), compliant walls (Hahn, Je & Choi 2002) and active blowing and suction (Kim 1999). Laminar drag reduction is much harder to achieve. Macroscale laminar drag reduction is possible with liquids, using surface or fluid electric charges (Maynes & Webb 2003) and via surface hydrophobicity (Tretheway & Meinhart 2002). Recent work (see Ou, Perot & Rothstein 2004; Ou & Rothstein 2005; Joseph *et al.* 2006) has shown that liquid laminar drag reduction is achievable in larger channels, using superhydrophobic surfaces (SHSs). SHSs combine hydrophobic chemistry with micron-scale topological features which can, in some cases, support a shear-free air–water interface resulting in slip lengths of the order of tens of microns in laminar flows.

In this work, we will demonstrate that SHSs can also produce significant drag reduction for liquids operating in the turbulent regime. Experiments by Gogte *et al.* (2005) using hydrophobically modified sand paper and recent results from Daniello, Waterhouse & Rothstein (2008) using precisely patterned hydrophobic microridges and microposts were at high enough Reynolds numbers to be turbulent and showed that drag reduction could be achieved. A theoretical analysis by Fukagata, Kasagi & Koumoutsakos (2006) suggests how a small alteration of the laminar sublayer can

---

† Email address for correspondence: perot@ecs.umass.edu

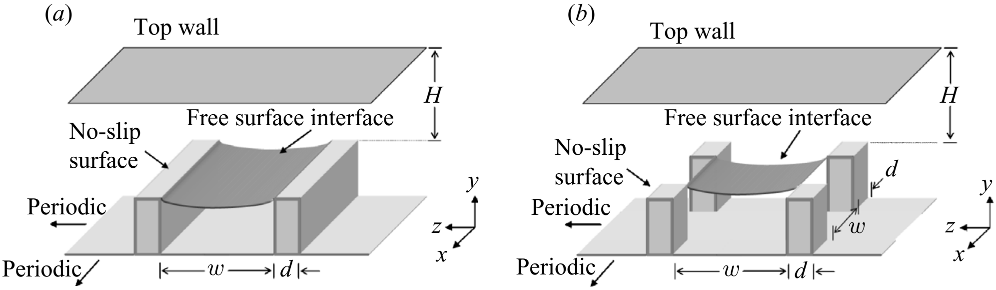

FIGURE 1. Schematic representations of the SHSs containing (*a*) ridges and (*b*) posts, arranged on a plane with periodic boundary conditions. The posts are square and spaced evenly in the streamwise (x) and spanwise (z) directions.

affect the entire turbulent boundary layer and subsequently alter the drag. Recently, Min & Kim (2004, 2005) performed a direct numerical simulation (DNS) in a channel at a friction Reynolds number $Re_\tau \approx 180$, in which the turbulence was fully resolved, but the SHS itself was modelled as an arbitrary slip length. Their simulations demonstrated a decrease in wall shear stress with increasing slip lengths both parallel and perpendicular to the flow direction. The surface boundary condition was modelled by the Navier slip condition, $u_{wall} = b(\partial u/\partial y)_{wall}$, where b is the slip length.

In the current work, both the turbulence and the surface boundary conditions are fully resolved, and the slip velocity is calculated for a number of SHS geometries. SHSs can be made using a variety of microfeatures. In this work, regular arrays of microridges and microposts are used, so that the microtopology is very well characterized. However, SHSs are also effective with random post arrangements (plasma etched plastics and the Lotus leaf being two common examples). The physical arrangements of microridge and micropost surfaces considered in this work are illustrated in figure 1. The SHS is only placed on the bottom wall of the channel.

The spacing and size of the microfeatures allows a shear-free liquid–gas interface to be supported between the individual posts or ridges. The gaps between posts or ridges allow a non-zero average slip velocity to be present on the surface and can result in drag reduction. Surface hydrophobicity keeps the liquid from advancing into the gaps between the surface features. While the chemical hydrophobicity of the surface (or its magnitude as measured by the static contact angle) has no affect on the drag reduction properties of the SHS, it does dictate the maximum pressure that the free surface can support before the free surface fails and the liquid is forced to move into the gap by static pressure (Ou *et al.* 2004).

In this investigation, only the liquid is simulated. The top surface of each microfeature is taken to be a no-slip boundary on the liquid, and the suspended liquid–gas interface between the microfeatures is simulated as a flat and shear-free boundary on the liquid. The streamwise and spanwise directions have periodic boundary conditions which approximate infinite parallel plates. While the drag is locally zero on the free surface between the posts or ridges, it is non-zero over the posts and ridges because of the no-slip boundary condition. The net drag is the sum of these two effects and depends on which effect dominates. While it is often stated that the drag reduction is a result of reduced wall contact with the fluid, this is an incomplete explanation of the phenomenon, as the spacing between the microfeatures is also critically important (Ou & Rothstein 2005).

The free surface in these simulations is assumed to experience no out-of-plane deflection. When the ratio of the deflection s and the gap width w is small, $s/w \ll 1$, the deflection can be well approximated by $s/w \approx (w\Delta p)/(8\sigma)$, where σ is the surface tension. For our maximum gap size of $90\,\mu\text{m}$ and water with $\sigma = 7\times10^{-2}\,\text{N}\,\text{m}^{-1}$, pressures up to 700 Pa can be supported with deflections less than 10 %. This spacing is near the upper limit of what can be effectively employed experimentally. The work of Ybert, Barentin & Cottin-Bizonne (2007) confirms that the effect deflections less than 20 % produce on laminar drag reduction is negligible. The assumption of shear-free flow on the free surface is reasonable if the posts and ridges are tall enough (i.e. of the same order of magnitude as the spacing). If the posts or ridges are significantly shorter than the gap width, then the circulating air in the gap between the microfeatures could result in drag on the free surface and cause such a surface to produce less drag reduction than what these DNS calculations predict.

2. Direct Numerical Simulations

A computational fluid dynamics (CFD) code was developed to perform DNS of turbulent channel flow over surfaces with varying boundary conditions. The governing Navier–Stokes equations are numerically solved using a second-order accurate Cartesian staggered mesh method with classical projection for the pressure solution. A second-order accurate, three-step, low-storage Runge–Kutta scheme is used to advance the solution in time. The mesh has non-uniform spacing in the vertical direction normal to the SHS, in order to allow greater resolution near the channel's top and bottom walls. A Cartesian mesh is well suited to the channel and the microfeature geometry being investigated. A staggered scheme is employed because it conserves mass, momentum, vorticity and kinetic energy. There is no numerical viscosity in this scheme (Perot 2000), which is vital to accurately predict the turbulent energy cascade (see Mittal & Moin 1998). The code is fully parallel, using MPI libraries, and is optimized for execution on supercomputers.

The computational domain is a box of ratio 6:2:3 (length:height:width). Here x is the streamwise direction of length L_x, y the vertical direction of height L_y and z the spanwise direction of width L_z. For the data presented in this paper, all resolutions have 128 grid points in each direction, except for two cases which have 256 grid points in each direction. These simulations were run at higher resolutions for validation purposes as discussed in § 3. The boundary conditions consist of alternating regions of no slip and no shear, which correspond to the top of the microfeature (a post or a ridge) and the interface supported between microfeatures, respectively. Periodic boundary conditions are employed in the streamwise (x) and spanwise (z) directions. Several ridge and post configurations were examined, where the feature width d and feature spacing w were varied (see figure 1). Eight ridges (in the spanwise direction) were present for all ridge simulations, except for one thin-ridge case which had 16 across the channel. Similarly, a minimum of eight posts in the spanwise direction, and sixteen in the streamwise direction, were present for all post simulations. Note that in the case of ridges, the configurations are referred to by the ratio of their spanwise width (in z) to spanwise spacing (in z). For example a ridge which is $30\,\mu\text{m}$ wide and spaced at $50\,\mu\text{m}$ is a '$30\,\mu\text{m}$–$50\,\mu\text{m}$ ridge'. All microridge cases investigated involve uniformly spaced ridges of equal width. Similarly, all micropost cases investigated involve square posts (whose widths d in both the streamwise and spanwise direction are equal) that are uniformly spaced (spacing w in both the streamwise and spanwise direction is equal). For clarity, the symbols used for each geometry remain consistent throughout the figures and are described in figures 3 and 5. In every case, the sum of each feature spacing and width ($w + d$) is kept constant at 8 grid points (in x) or 16 grid points (in z) and 67.5^+ wall units for simulations with 128^3 grid points at a friction Reynolds number $Re_\tau \approx 180$, with the noted exceptions of the 15 μm–15 μm ridges and resolution independence simulation. At the Reynolds number simulated in this work, the surface microfeatures and gaps have sizes ranging from 17^+ wall units wide to 50^+ wall units wide. At their largest, the feature widths and gaps are below the streak width of 100^+ wall units.

The instantaneous variables calculated in the CFD code are averaged. As such, each subdomain around a single feature produces a set of temporally averaged velocity and pressure data, denoted $\bar{u}^t$ and $\bar{p}^t$. These temporal averages are then ensemble averaged and denoted by angle brackets $\langle\rangle$ over all the posts or ridges in the simulation to produce $\langle\bar{u}^t\rangle$ and $\langle\bar{p}^t\rangle$. The Reynolds stresses are calculated as $\boldsymbol{R}(x, y, z) = \langle\overline{(u_i - \langle\bar{u}^t\rangle)(u_j - \langle\bar{u}^t\rangle)}^t\rangle$. For graphical presentation, we calculate velocity averages over x–z planes to remove the local microfeature variations,

$$U(y) = \overline{\langle\bar{u}^t\rangle}^{xz} = (1/L_x L_z)\int_0^{L_x}\int_0^{L_z}\langle\bar{u}^t\rangle\,\mathrm{d}x\mathrm{d}z.$$

Similarly, the planar-averaged Reynolds stresses are $R_{ij}(y) = \overline{\boldsymbol{R}}^{xz} = (1/L_x L_z)\int_0^{L_x}\int_0^{L_z}\boldsymbol{R}\,\mathrm{d}x\,\mathrm{d}z$. Finally, the bulk velocity

$$U_{bulk} = (1/L_y)\int_{-L_y/2}^{+L_y/2} U(y)\,\mathrm{d}y$$

is used as a velocity scale, noting the centre of the channel is located at $y = 0$. The slip velocity, $U_{slip} = U(-L_y/2)$ is the x–z planar average of the streamwise velocity at the lower wall. This slip velocity is a macroscopic value, as the actual velocities at the SHS are either zero (above the no-slip feature) or some non-zero value (above the interface). The average wall shear stress $\tau_w = (\tau_w^T + \tau_w^B)/2$ is calculated by averaging the top wall shear stress $\tau_w^T = \mu(\partial U/\partial y)_{y=L_y/2}$ and the bottom wall shear stress $\tau_w^B = \mu(\partial U/\partial y)_{y=-L_y/2}$, where μ is the viscosity. The top and bottom wall shear stresses are also macroscopic quantities. At statistical steady state, the average wall shear stress τ_w is directly related to the average channel pressure gradient $(\partial P/\partial x)$ by $\tau_w = (2/L_y)(\partial P/\partial x)$. Note the pressure gradient, not the mass flux, is prescribed in these calculations.

3. Validation

Considering no analytical solution is available for turbulent flow over SHS, a simulation of laminar flow over boundary conditions similar to those employed for an SHS was performed as a means of validating the boundary conditions. Velocity profiles from a simulation with a single shear-free gap in a no-slip plate were compared with the solution for low-Reynolds-number flow between two parallel plates with a single streamwise no-shear band in the bottom plate, as calculated analytically by Philip (1972) and presented in Lauga & Stone (2003). In figure 2(*a*), the velocity profiles above the shear-free and no-slip regions are shown. Excellent agreement between the analytical solution and the simulation results is found.

Previous DNS of turbulent channel flow performed by Moser, Kim & Mansour (1998) was employed as a means of validating the CFD code in the turbulent regime. In figure 2(*c*, *d*), the planar-averaged streamwise velocity profile and the four non-zero planar-averaged Reynolds stresses are compared to the results of Moser *et al.* (1998) with quantitative agreement at a friction Reynolds number of $Re_\tau = (u_\tau L_y)/2\nu = 180$. The friction velocity is given by $u_\tau = (\tau_w/\rho)^{1/2}$. The results are plotted against the non-dimensional channel height $y^+ = u_\tau y/\nu$, where y is the vertical position in the

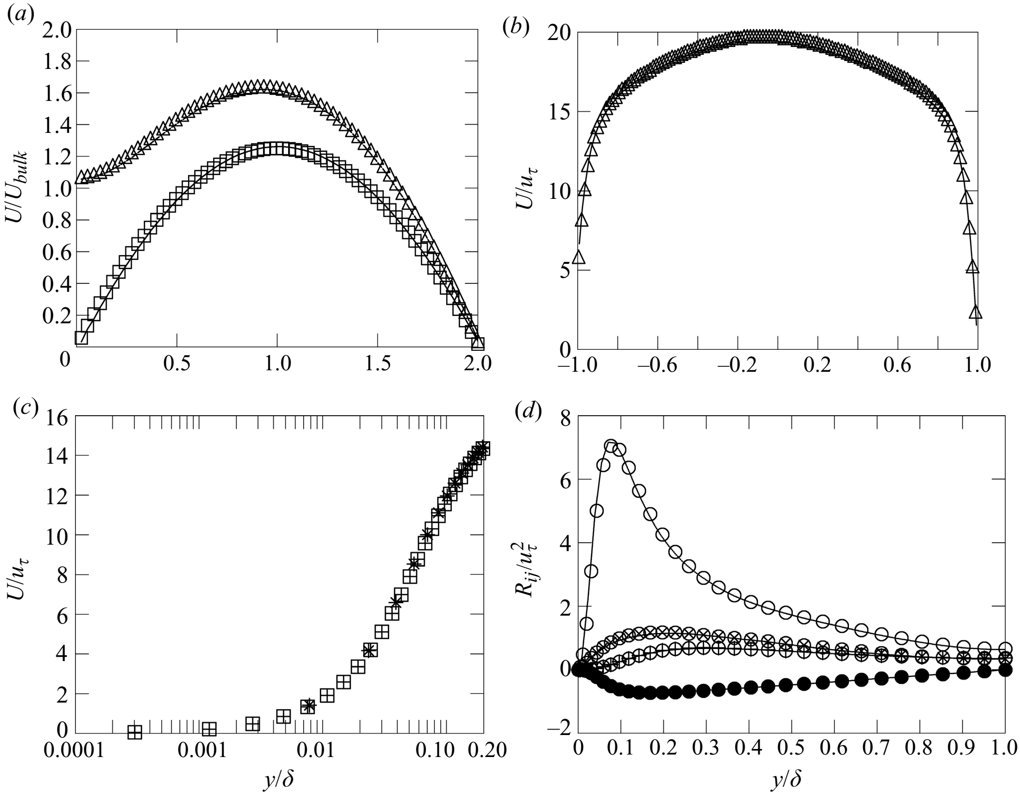

FIGURE 2. (*a*) Laminar validation for flow over a single streamwise shear-free band in a no-slip plate, compared with analytical solution from Philip (1972). Velocity profiles are shown above the no-slip region in the simulation (—) and the centre of the shear-free region (– –) and compared to the predictions of the analytical solution for the no-slip (□) and shear-free (△) regions. (*b*) Velocity profiles from turbulent flow over ridges at $Re_\tau \approx 180$, performed with resolutions of 128^3 (—) and 256^3 (△), demonstrating the resolution independence of the DNS. (*c*) Velocity profiles and (*d*) Reynolds stresses calculated with the present code ($*$ and $\cdots$, respectively) for turbulent channel flow at $Re_\tau \approx 180$ compared with results of Moser *et al.* (1998), including U/u_τ (⊞), R_{11}(○), R_{22}(⊕), R_{33}(⊗) and R_{12}(●).

channel. Note that the left end of the axis in figure 2(d) corresponds to the bottom wall of the channel and the right end corresponds to the centre of the channel. For standard channel flow, the velocity and Reynolds stress profiles are symmetric about the channel's centre plane. This assumption of symmetry does not apply to the subsequent simulations of channels with a superhydrophobic lower surface and standard upper surface. Validation was also performed to ensure the SHS features are properly resolved at the grid resolution employed for these cases. In figure 2(*b*), velocity profiles from turbulent channel flow at $Re_\tau \approx 180$ are shown over the same 30 µm–30 µm ridges at resolutions of 128^3 and 256^3. The velocity profiles and Reynolds stresses (see code validation and resolution independence studies in Martell 2008) agree to within 3 %, indicating that the features are well resolved at 128^3.

4. Results

Velocity profiles and Reynolds stresses were computed for the four different ridge cases considered. Figure 3(*a*) shows the mean velocity profiles normalized by the

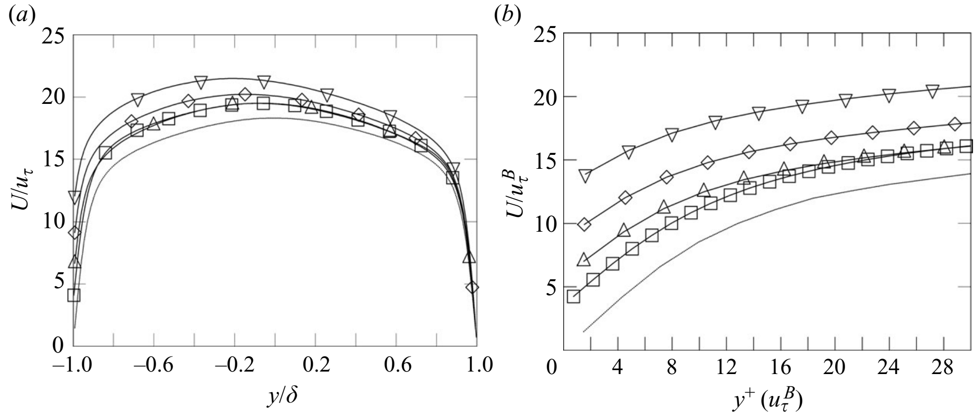

FIGURE 3. Planar-averaged velocity profiles for flow over SHS with ridges. The data includes 15 μm–15 μm (□), 30 μm–30 μm (△), 30 μm–50 μm (◇) and 30 μm–90 μm (▽) ridges, with smooth channel flow (· · ·). (*b*) A close up of the SHS is shown to highlight slip. Symbols are employed to differentiate lines and do not necessarily reflect actual data points.

average friction velocity u_τ. The channel height (y) is normalized by the channel half-height $\delta = L_y/2$. The smooth channel flow data are provided for reference. Results from the ridge cases show slip velocities and peak mean velocities that increase with increased width to spacing ratio d/w. In addition, the peak velocity moves closer to the SHS. In figure 3(*b*), the velocity profiles are shown close to the SHS and plotted against y^+. In this figure both axes are scaled by the bottom wall shear stress τ_w^B. The 15 μm–15μm ridge case was performed with 256 grid points in each direction for validation purposes, explaining the presence of a data point closer to the SHS. It is interesting to note that in figure 3(*a*) the velocity profiles for 15 μm–15 μm and 30 μm–30 μm ridges cross at roughly $y/\delta = -0.8$ ($y^+ \approx 28$). This appears to be a characteristic of the flow, resulting from the interplay of the slip velocity and the subsequent asymmetry in the velocity profile and not a resolution issue, as the profile for 30 μm–30 μm ridges at twice the resolution (256^3) is nearly identical to the one presented in the figure (see figure 2*b*).

The Reynolds stresses $R_{ij}(y)$ resulting from turbulent flow over an SHS with ridges are shown in figure 4 and are scaled by the average friction velocity squared, u_τ^2. Since the mean pressure gradient remains constant in these simulations, a net reduction in drag or shear on the superhydrophobic boundary leads to a corresponding increase in the net shear on the smooth wall. With reduced shear, turbulence levels decrease near the superhydrophobic boundary. The turbulence levels increase on the no-slip boundary because of the higher shear now present near the upper wall. In the middle of the channel, the slope of the shear stress (R_{12}) must balance the fixed pressure gradient, resulting in curves that are all parallel in this region. Note that, due to the slip velocities present in the x and z directions, R_{11} and R_{33} become non-zero at the SHS. The peak values of R_{11}, R_{22} and R_{33} decrease near and are shifted towards the SHS, resulting in an asymmetric Reynolds stress profile. These effects are all found to increase with increasing spacing and slip velocity.

Figures 5 and 6 show $U(y)$ and $R_{ij}(y)$ for turbulent flow over an SHS with posts. Similar to the results found with ridges, the slip velocities and peak mean velocities for the post cases increase with increase in d/w. For posts, the slip velocities tend to be larger than those from equivalently sized or spaced ridges. Similar to results found

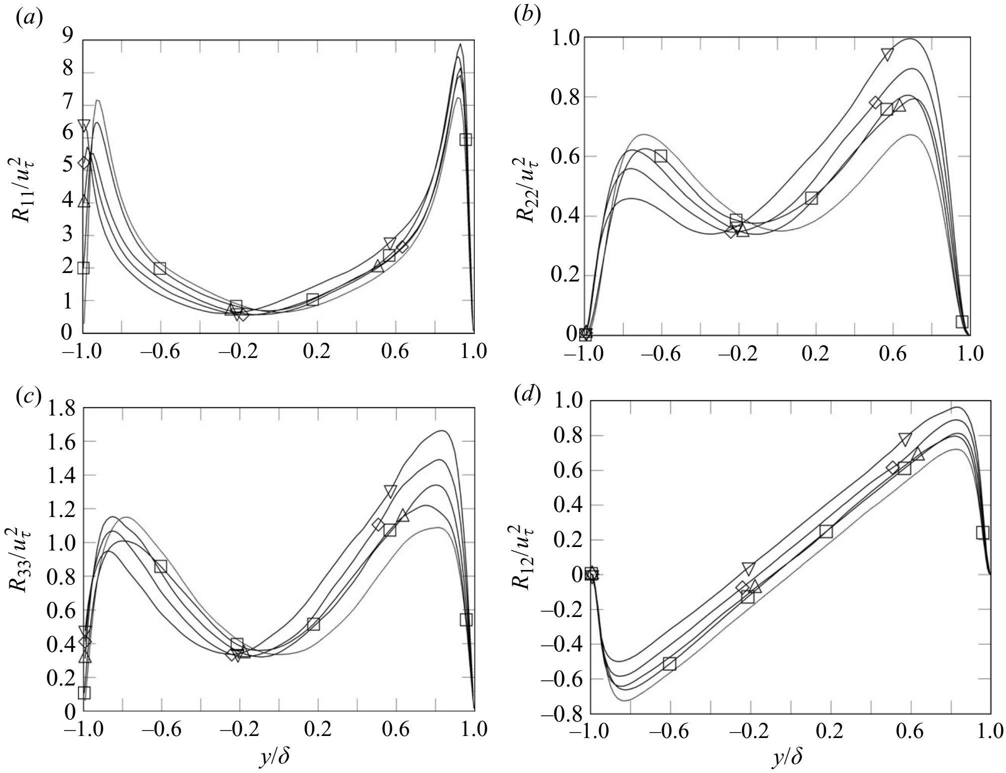

FIGURE 4. Reynolds stress profiles for turbulent flow past SHS with ridges. The symbols and lines are the same as those employed in figure 3.

with ridges, R_{11} becomes non-zero at the SHS, and its peak value decreases near the SHS. The asymmetry present in R_{11} is more pronounced in the post cases than in the ridge cases. In addition, the peak in R_{11} for both the 30 μm–50 μm and 30 μm–90 μm post cases moves so that the maximum occurs on the SHS itself.

5. Discussion

The presence of SHS microfeatures has a significant affect on the behaviour of turbulent channel flow. Marked changes in the velocity profiles, Reynolds stresses and wall shear stress are observed for a variety of microridge and micropost geometries. These results are consistent with the recent experimental work of Daniello *et al.* (2008), who have investigated turbulent flow over SHSs with similar microfeature geometries.

Figures 3(*b*) and 5(*b*) suggest that the essential scaling properties of turbulent boundary layers remain intact even when an SHS is present and significant drag reduction is occurring for that boundary layer. In those figures, $u^+ = C + y^+$ (where C is the normalized slip velocity) to within 10 % for all the cases considered. For this result it was important to scale with the local (bottom) boundary shear stress. Figure 7 investigates if this scaling holds for the turbulence as well as the mean flow. This figure shows R_{12} profiles for all investigated seven cases scaled by the bottom wall shear stress. The profiles all collapse onto the standard channel flow profile near the bottom wall (SHS), suggesting that the structure of the near-wall turbulence has

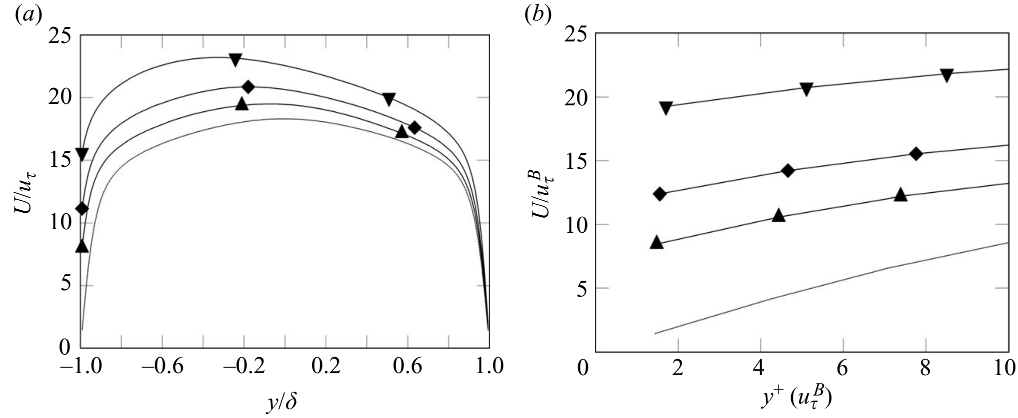

FIGURE 5. Planar-averaged velocity profiles for turbulent flow over the SHS with posts. The data include 30 µm–30 µm (▲), 30 µm–50 µm (◆) and 30 µm–90 µm (▼) posts, with smooth channel flow (· · ·). (*b*) The velocity profiles near the SHS are expanded to emphasize the slip velocity. Symbols are employed to differentiate lines and do not necessarily reflect actual data points.

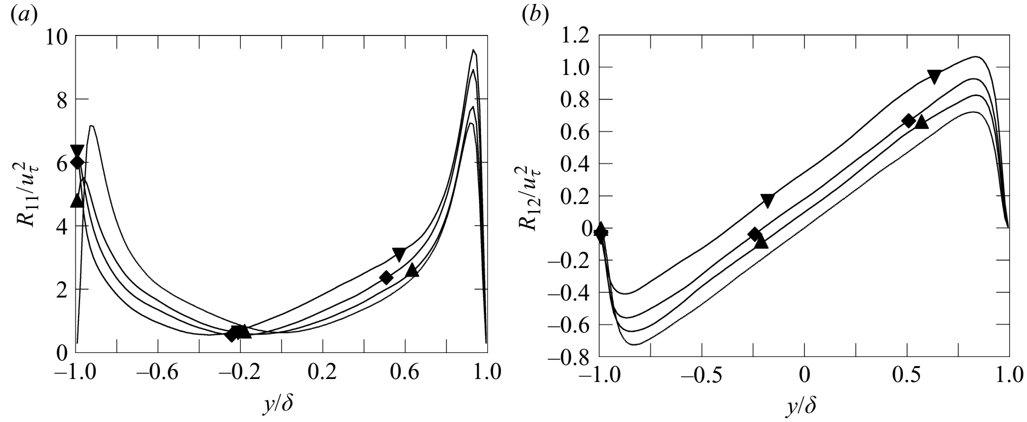

FIGURE 6. Reynolds stress profiles for turbulent flow past SHS with posts. Symbols and lines are the same as those employed in figure 5.

not fundamentally changed. Less surprisingly (and not shown), the same behaviour is also exhibited at the top wall if the R_{12} profiles are scaled by the top wall shear stress.

The slip and drag reduction properties of the SHS are summarized in figure 8. Drag reduction performance increases with increased feature spacing. This trend is consistent for both ridges and posts, as the slip velocity attains a maximum nearly 65 % of the bulk velocity for ridges and over 75 % of the bulk velocity for posts, with a width to spacing ratio d/w just above 0.3. For ridge width to spacing ratios $d/w = 1$, more slip is achieved with larger microfeature widths and gaps. This is clearly seen in figure 8(*a*), where the slip velocity for 15 µm–15 µm ridges is nearly 40 % lower than the slip velocity for the 30 µm–30 µm ridges. A similar trend for the

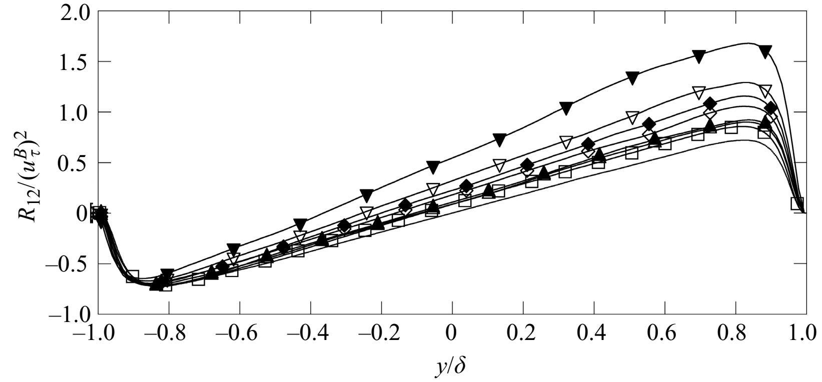

FIGURE 7. Reynolds stress profiles, R_{12}, for flow past SHS with streamwise ridges and square uniformly spaced posts, showing a collpase at the SHS when scaled by the square of the bottom wall friction velocity, $(u_\tau^B)^2$. Symbols and lines are the same as those employed in figures 3 and 5.

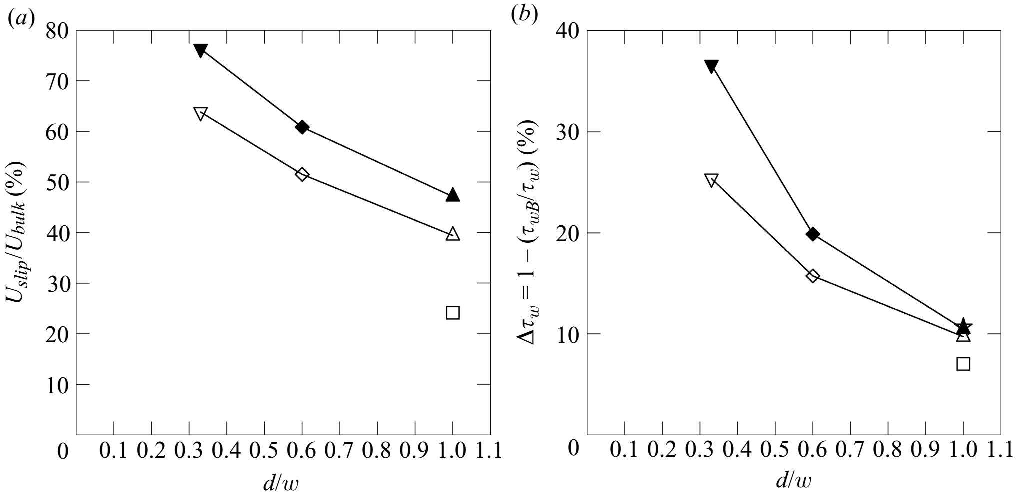

FIGURE 8. Turbulent drag reduction performance of the SHS for both ridges and posts as a function of the width to spacing ratio. (*a*) Slip velocity at the SHS normalized by the bulk velocity for varying feature width and spacing. (*b*) Wall shear stress reduction at the SHS, normalized by the average wall shear stress, for varying feature width and spacing. The data include 15 µm – 15 µm (□), 30 µm – 30 µm (△), 30 µm – 50 µm (◇) and 30 µm – 90 µm (▽) ridges, as well as 30 µm – 30 µm (▲), 30 µm – 50 µm (◆) and 30 µm – 90 µm (▼) posts. A result from Daniello *et al.* (2008) is superimposed (★) over the simulation data in (*b*).

drag reduction is found in figure 8(*b*), where the bottom wall shear stress reduction for the 15 µm–15 µm ridges is nearly 30 % lower than that for 30 µm–30 µm ridges. This is consistent with the observations made by Ou & Rothstein (2005). Experimental data from Daniello *et al.* (2008) (not shown) observes similar trends for features with identical d/w ratios but different sizes (15 µm–15 µm versus 30 µm–30 µm ridges for simulations and 30 µm–30 µm versus 60 µm–60 µm ridges for experimental data), where thinner feature widths and gaps show less drag reduction and lower slip velocities (see figure 8*a*, *b*). This indicates that the actual size of the features, and not simply the ratio of width to spacing (or the percentage of shear-free surface on the SHS), plays an important role in the surface's drag reduction. Smaller features lead to diminished drag-reduction performance. Also note the close agreement with 30 μm–30 μm ridge data from Daniello *et al.* (2008) at the same Reynolds number superimposed over the simulation data in figure 8(*b*), which shows the same shear stress reduction as predicted by simulation. Small differences in wall shear stress reduction may be attributed to experimental error or the slight disparity between the geometries employed in the experiments and simulations.

When comparing posts and ridges, it is clear that for a given ratio of microfeature size to spacing, d/w, posts yield higher slip velocities and larger shear stress reductions. The performance advantage of posts over ridges appears to increase with increased feature spacing.

The authors would like to thank the Office of Naval Research for support of this research under grant N00014-06-1-0497.

REFERENCES

Bechert, D. W., Bruse, M., Hage, W., VanderHoeven, J. G. T. & Hoppe, G. 1997 Experiments on drag-reducing surfaces and their optimization with an adjustable geometry. *J. Fluids Mech.* **338**, 59–87.

Daniello, R., Waterhouse, N. E. & Rothstein, J. P. 2008 Turbulent drag reduction using superhydrophobic surfaces. Submitted to *Phys. Fluids.*

Fukagata, K., Kasagi, N. & Koumoutsakos, P. 2006 A theoretical prediction of friction drag in turbulent flow by superhydrophobic surfaces. *Phys. Fluids* **18**, 051703:1–051703:4.

Gogte, S., Vorobieff, P., Truesdell, R., Mammoli, A., van Swol, F., Shah, P. & Brinker, C. J. 2005 Effective slip on textured superhydrophobic surfaces. *Phys. Fluids* **17**, 051701:1–051701:4.

Hahn, S., Je, J. & Choi, H. 2002 Direct numerical simulation of turbulent channel flow with permeable walls. *J. Fluid Mech.* **450**, 259–285.

Joseph, P., Cottin-Bizonne, C., Benot, J.-M., Ybert, C., Journet, C., Tabeling, P., & Bocquet, L. 2006 Slippage of water past superhydrophobic carbon nanotube forests in microchannels. *Phys. Rev. Lett.* **97** (15), 156104.

Kim, J. 1999 Active control of turbulent boundary layers for drag reduction. *Lect. Notes Phys.* **529**, 142–152.

Lauga, J. & Stone, H. 2003 Effective slip in pressure-driven stokes flow. *J. Fluid Mech.* **489**, 55–77.

Lumley, J. L. 1969 Drag reduction by additives. *Annu. Rev. Fluid Mech.* **1**, 367.

Martell, Michael B. 2008 Simulations of turbulence over ultrahydrophobic surfaces. Master's thesis, The University of Massachusetts, Amherst, MA.

Maynes, D. & Webb, B. W. 2003 Fully developed electro-osmotic heat transfer in microchannels. *Intl J. Heat Mass Transfer* **46** (8), 1359–1369.

Min, T. & Kim, J. 2004 Effects of hydrophobic surface on skin-friction drag. *Phys. Fluids* **16** (7), L55–L58.

Min, T. & Kim, J. 2005 Effects of hydrophobic surface on stability and transition. *Phys. Fluids* **17**, 108106:1–108106:4.

Mittal, R. & Moin, P. 1998 Suitability of upwind-biased finite difference schemes for large-eddy simulation of turbulent flows. *Am. Inst. Aeronaut. Astronaut. J.* **35** (8), 1415–1417.

Moser, R., Kim, J. & Mansour, N. 1998 Direct numerical simulation of turbulent channel flow up to $Re_\tau = 590$. *Phys. Fluids* **11** (4), 943–945.

Ou, J., Perot, J. B. & Rothstein, J. 2004 Laminar drag reduction in microchannels using superhydrophobic surfaces. *Phys. Fluids* **16** (12), 4635–4643.

Ou, J. & Rothstein, J. 2005 Direct velocity measurements of the flow past drag-reducing ultrahydrophobic surfaces. *Phys. Fluids* **17** (10), 13606:2–13606:10.

Perot, J. B. 2000 Conservation properties of unstructured staggered mesh schemes. *J. Comput. Phys.* **159**, 58–89.

Philip, J. R. 1972 Integral properties of flows satisfying mixed no-slip and no-shear conditions. *J. App. Math. Phys. (ZAMP)* **23**, 960–968.

Tretheway, D. C. & Meinhart, C. D. 2002 Apparent fluid slip at hydrophobic microchannel walls. *Phys. Fluids* **14** (3), L9–L12.

Ybert, C., Barentin, C. & Cottin-Bizonne, C. 2007 Acheiving large slip with superhydrophobic surfaces: Scaling laws for generic geometries. *Phys. Fluids* **19**, 123601:1–123601:10.